Available online at www.easd.procedia.org
EASD Procedia EURODYN (2026) 887-901
Davide Spitaleri, Gianluca Pepe, Maicol Laurenza, Enrico M. Di Pietro, Antonio Carcaterra

EASD Procedia

EURODYN 2026
XIII International Conference on Structural Dynamics
M. Beer, C. Papadimitriou, H. Jensen, J. Chen, M. Broggi, J. Behrensdorf (eds.)
Hannover, Germany, 27.09.–01.10 2026

ATHMOS: EXPERIMENTAL VALIDATION AND HYBRID MOBILITY CONTROL OF A SPHERICAL AERIAL-GROUND ROBOT

Davide Spitaleri[1], Gianluca Pepe[1], Maicol Laurenza[2], Enrico M. Di Pietro[1] and Antonio Carcaterra[1]

[1] Department of Mechanical and Aerospace Engineering, University "La Sapienza",
Eudossiana Street, 18, Rome, Italy
{davide.spitaleri, gianluca.pepe, enricomaria.dipietro.guest, antonio.carcaterra}@uniroma1.it

[2] Department of engineering, Niccolò Cusano University
Don Carlo Gnocchi Street, 3, Rome, Italy
maicol.laurenza@unicusano.it

Keywords: Hybrid aerial-ground robot, Spherical robot, Nonlinear control, Model-based Control, Experimental validation.

Abstract. *This paper presents the experimental validation of ATHMOS a spherical hybrid aerial–ground robot designed for confined, contact-rich environments that combines energy-efficient terrestrial rolling with agile aerial locomotion. A mode-dependent model-based control and state estimation architecture is implemented to manage flight, rolling, mode transition phases and contact interactions, dominated by nonlinear phenomena. We experimentally validated the current prototype through repeatable outdoor tests covering rolling and flying segments, take-off, landing, and transition maneuvers. Reported metrics include tracking performance, state estimation accuracy, transition response times, contact-detection reliability, and energy per distance in rolling versus low-speed flight. The results confirm the feasibility of using rolling as the primary energy-efficient locomotion mode and flight as a complementary mode for obstacles, discontinuities, and three-dimensional maneuvers, overcoming the trade-off between agility, contact robustness, and energy efficiency. The contribution offers a reproducible methodology, hybrid control logic, and experimental protocols, for early-stage evaluation of spherical aerial–ground robots operating under nonlinear dynamics and intermittent environment interaction.*

ISSN:2311-9020 © 2026 The Authors. Published by EASD Procedia.
Peer-review under responsibility of the Organizing Committee of EURODYN 2026.
doi: 10.47964/1326.10705.206

1 INTRODUCTION

Hybrid aerial–ground robots have attracted increasing interest for application such as inspection, monitoring, exploration, and search-and-rescue in environments where purely terrestrial or purely aerial robots face significant limitations. Ground locomotion is generally more energy efficient and safer near obstacles, while flight provides three-dimensional mobility and the ability to overcome obstacles and discontinuities. However, the development of these hybrid robots still faces a challenging design trade-off between efficiency and agility, as well as between versatility and mechanical simplicity [1].

Several hybrid architectures have been proposed to combine aerial and ground locomotion, including reconfigurable robots, wheeled or passively rolling platforms, and vehicles exploiting shared actuation systems [2-5]. Nevertheless, many of these solutions are hampered by mechanical complexity, poor transition agility and reliability, or limited robustness to impacts. A particularly relevant class for confined and contact-rich environments is represented by aerial–ground robots equipped with an external cage, where the protective structure also serves as the physical interface for terrestrial locomotion. Pioneering solutions such as HyTAQ demonstrated that enclosing a conventional quadrotor within a rolling cage can substantially extend operational endurance by exploiting ground locomotion while preserving the ability to fly over obstacles [6]. However, in such architectures the multirotor remains fundamentally underactuated, and rolling is obtained indirectly by tilting the thrust vector. As a consequence, ground motion and contact interaction remain strongly coupled to vehicle attitude, limiting terrestrial maneuverability. To improve the controllability of ground motion, spherical or quasi-spherical solutions have been proposed, including variable-pitch propellers [7], compact rolling–flying platforms [8] and systems designed for inspection in confined environments [9]. Other architectures introduce mechanical decoupling between the flying platform and the outer shell, for instance through passive cages or gimbal mechanisms, in order to reduce the effects of impacts on vehicle dynamics and enable more omnidirectional terrestrial mobility [10-12]. These solutions can improve controllability and contact robustness, but they also introduce increased mechanical complexity, moving interfaces, calibration requirements and potential fragility in harsh or debris-rich environments.

In this framework, rigidly integrated and over-actuated spherical architectures represent an alternative approach: rather than decoupling the shell from the aerial platform, the spherical cage and the propulsion system are treated as a single controlled rigid body. This configuration is particularly promising for combining omnidirectional rolling, high control authority, robust contact interactions and rapid transitions between terrestrial and aerial locomotion. Previous concepts such as Rollocopter have highlighted the energy and mobility advantages of this class of systems with preliminary numerical validations, but with limited experimental evidence on real prototypes [13].

The present work addresses this gap by introducing ATHMOS (Aerial-Terrestrial Hybrid Mobility Omnidirectional Sphere), a rigidly integrated hybrid spherical robot based on an overactuated multirotor architecture. The system is designed to combine efficient terrestrial locomotion, omnidirectional mobility, collision tolerance, and high aerial agility in a compact and robust platform. Overactuation ensures high control authority across the different operating modes, while the spherical cage enables omnidirectional rolling and protects the components during impacts and falls. This combination makes ATHMOS particularly well-suited to confined, unstructured and contact-rich environments, where it can prioritize rolling over long distances and reserve flight only when three-dimensional mobility is truly required, with potential benefits for the overall energy efficiency of the mission.

To handle omnidirectional locomotion, transitions, and impacts, which are characterized by hybrid and highly non-linear dynamics, we propose a model-based control algorithm that combines constrained dynamic allocation with the Feedback Local Optimality Principle, belonging to the class of Variational Feedback Controllers developed by our research group [14-16]. In a previous study, we numerically validated the system's potential in a multibody environment [17]. In this article, we describe the ATHMOS prototype and present experimental validation in realistic scenarios, including tests of autonomous rolling, take-off, landing and mode transition. The results also show that continuous ground contact can improve state estimation even under degraded GNSS conditions, increasing the robustness of autonomous navigation in complex and confined environments.

The remainder of the paper is organized as follows. Section 2 describes the mechatronic design of ATHMOS. Section 3 presents the control and state estimation architecture of the system. Section 4 reports the results from experimental campaign. Section 5 concludes the paper and provides future developments.

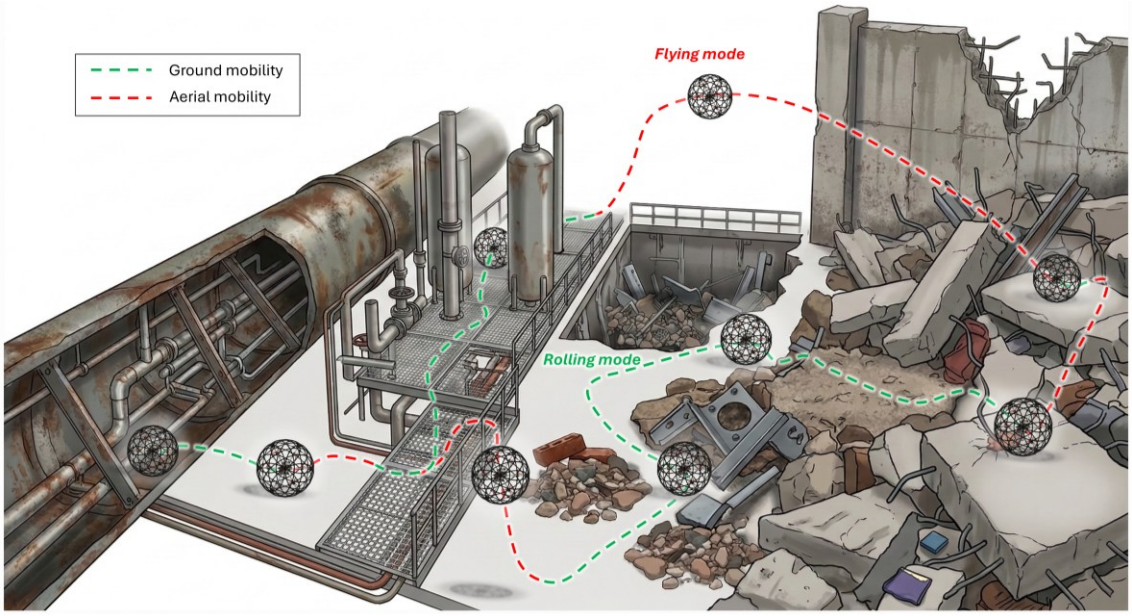


Figure 1: The illustration depicts ATHMOS's main operational scenarios, highlighting the complementary nature of ground and aerial mobility in confined, industrial, and unstructured SAR environments.

2 MECHATRONIC DESIGN

ATHMOS is a hybrid aerial–ground robot composed of an overactuated multirotor rigidly integrated inside an external spherical shell. The prototype is shown in Figure 2 and has a total mass of approximately 2.7 kg and an external radius of about 0.30 m. It is designed to combine flight, omnidirectional rolling, and impact tolerance in a compact mechanical structure. The mechanical architecture consists of three main subsystems: a central unit, housing the battery, sensors and onboard electronics; a cubic load-bearing frame, supporting the propulsion system and built from aluminum tubular elements; and a spherical shell, manufactured as a 3D-printed PLA lattice. The latter not only serves as a protective function but also acts as physical interface for terrestrial locomotion: the spherical geometry allows uniform rolling in every direction, while preserving a regular external shape suitable for interactions with walls, obstacles, and irregular surfaces. The propulsion system uses eight rotors mounted along the diagonals of the cubic frame, following the principle of omnidirectional multirotor architectures [18]. Unlike a conventional quadrotor, this arrangement provides greater flexi-

bility in generating forces and torques, improving control authority in flight, roll and transition phases. Each motor is equipped with a 6-inch bidirectional propeller with a symmetric profile, allowing thrust generation in both directions: this enlarges the set of achievable actions and makes the response more uniform across different control directions.

The onboard avionics are based on a Pixhawk 6C flight controller running PX4 firmware [19], integrating redundant inertial sensors, magnetometer, and barometer. For outdoor navigation, the prototype uses two multiband GNSS receivers with RTK support. These are mounted in diametrically opposite positions inside the spherical shell to improve sky visibility during rolling and reduce interference from the central electronics. Power is supplied by a 6S 3300 mAh LiPo battery. Communication with the ground station is provided through a telemetry radio and a dedicated remote-control link.

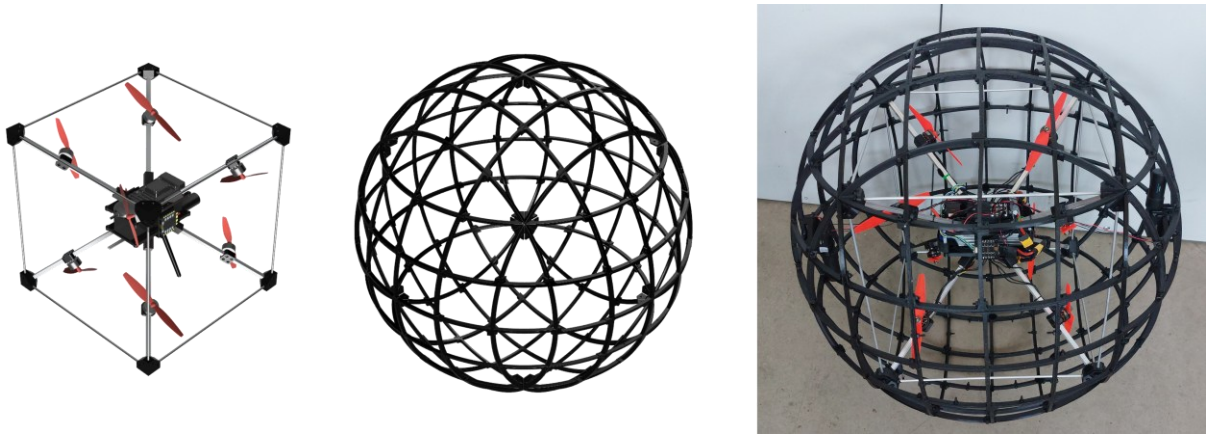


Figure 2: ATHMOS mechatronic architecture, showing the overactuated eight-rotor propulsion system, the cubic load-bearing frame, and the external spherical lattice shell. The shell provides both impact protection and the rolling interface for omnidirectional terrestrial locomotion, while the internal unit hosts the onboard electronics, battery, and navigation sensors.

3 MODEL-BASED CONTROL ARCHITECTURE

The state estimation and control architecture for ATHMOS autonomous navigation is represented in Figure 3. It is organized as a feedback loop that tracks a target trajectory $\boldsymbol{x}_T$, estimates the current vehicle's state $\boldsymbol{x}_{est}$ and active dynamic mode, and computes the required control action. The architecture consists of three main blocks. The first one performs state estimation and operating mode identification by fusing onboard sensor measurements and detecting contact with the ground. The second block implements the nonlinear model-based controller, which computes the generalized action to minimize the tracking error with respect to the target trajectory, utilizing a reference model selected according to the identified locomotion mode. The third block performs constrained allocation, mapping the desired generalized action to the eight motor commands while respecting actuator limits. This mode-dependent architecture allows for a unified approach for both locomotion modes, while maintaining distinct dynamic models for flight and rolling. The reference model therefore plays a key role: it must properly describe the vehicle's main nonlinearities, including contact dynamics and rolling constraints, while remaining compact enough to allow real-time execution on the onboard hardware.

The following sections describe, respectively, the dynamic model adopted, the contact estimation and detection strategy, and the nonlinear control law with constrained allocation.

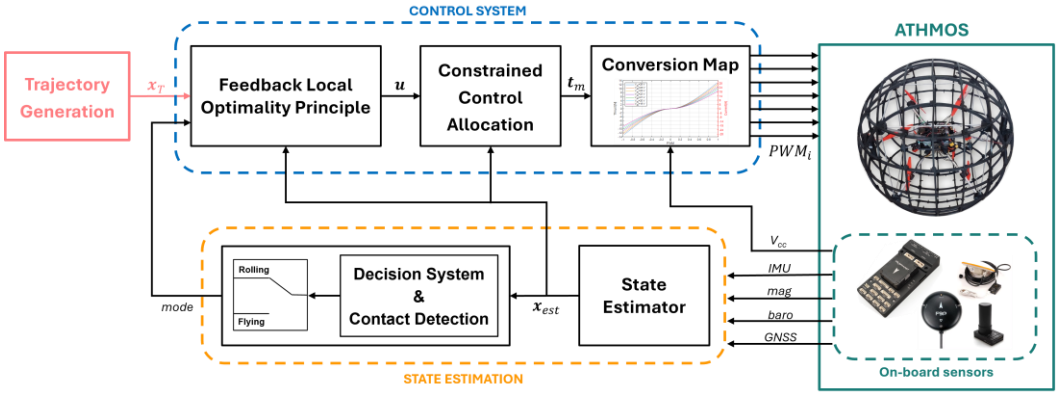


Figure 3: Model-based estimation and control architecture for ATHMOS. The target trajectory is tracked by estimating the vehicle state and locomotion mode, selecting the appropriate flight or rolling reference model, computing the nonlinear control action, and allocating it to the eight rotors under actuator constraints.

3.1 Reference model

The hybrid behavior of ATHMOS is described by two distinct dynamic models, derived from the Euler-Lagrange formulation. The flight model describes the rigid-body translational and rotational dynamics of the aerial vehicle, accounting for the propulsive actions produced by the rotors. The rolling model additionally includes the constraints related to ground contact. In both cases, the rotor dynamics and their coupling effects with the chassis are neglected, as these typically contribute only marginally or decay rapidly compared to the dynamics of the entire vehicle, resulting at the end in a streamlined model suitable for real-time control.

The reference model is formulated using generalized coordinates:

$$\boldsymbol{\eta} = [x, y, z, q_0, q_1, q_2, q_3]^\top \tag{1}$$

Where $\boldsymbol{r} = [x\ y\ z]^\top$ is the position of the center of mass G, assumed coincident with the geometric center of the spherical shell, and $\boldsymbol{q} = [q_0, q_1, q_2, q_3]^\top$ is the unit quaternion describing the attitude of the body frame $\{b\}$ with respect to the inertial frame $\{n\}$, following the North-East-Down (NED) convention. Unless otherwise indicated by superscript, vectors and tensors are expressed in the inertial frame in the following discussion. The use of quaternion representation avoids kinematic singularities and naturally adapts to omnidirectional spherical motion. Accordingly, rotational kinematics is expressed through the rotation matrix $\boldsymbol{R}_b^n(\boldsymbol{q})$ and the transformation matrix $\boldsymbol{E}(\boldsymbol{q})$, which relates the quaternions derivative to the angular velocity according to the relation [20]:

$$\boldsymbol{\omega} = 2\boldsymbol{E}(\boldsymbol{q})^\top \dot{\boldsymbol{q}} \tag{2}$$

The kinetic and potential energy of the system are:

$$\begin{aligned} T &= \frac{1}{2} m \dot{\boldsymbol{r}}^\top \dot{\boldsymbol{r}} + \frac{1}{2} \boldsymbol{\omega}^\top \boldsymbol{R}_b^n \boldsymbol{I}^b \boldsymbol{R}_n^b \boldsymbol{\omega} \\ U &= -m \boldsymbol{r}^\top \boldsymbol{g} \end{aligned} \tag{3}$$

Where $\boldsymbol{g} = [0\ 0\ g]^\top$ is the gravitational acceleration vector, m is the robot mass and $\boldsymbol{I}^b$ is the inertia tensor expressed in the body frame, assuming an equivalent disk model for the rotors. Defining the Lagrangian of the system $\mathcal{L}$ as the difference between kinetic and potential energy, we can formulate the augmented Lagrangian $\mathcal{L}^*$ by incorporating the constraint equations ψ_k via Lagrange multipliers λ_k:

$$\mathcal{L}^*(\boldsymbol{\eta}, \dot{\boldsymbol{\eta}}, \lambda, t) = T - U + \lambda_q \psi_q(\boldsymbol{\eta}) + \lambda_c \psi_c(\boldsymbol{\eta}) + \boldsymbol{\lambda}_r^\top \boldsymbol{\psi}_r(\boldsymbol{\eta}, \dot{\boldsymbol{\eta}}) \tag{4}$$

The introduced constraints are three: the quaternion unit norm constraint ψ_q, the contact constraint with a planar support surface ψ_c, and the pure rolling kinematic constraint $\boldsymbol{\psi}_r$ relating horizontal and angular velocities. The first is always active, while the other two are active only during rolling locomotion on ground.

$$\begin{aligned} \psi_q(\boldsymbol{\eta}) &= \boldsymbol{q}^\top \boldsymbol{q} - 1 = 0 \\ \psi_c(\boldsymbol{\eta}) &= z - R = 0 \\ \boldsymbol{\psi}_r(\boldsymbol{\eta}, \dot{\boldsymbol{\eta}}) &= \begin{bmatrix} \dot{x} - 2R(\dot{q}_0 q_2 - \dot{q}_1 q_3 - \dot{q}_2 q_0 + \dot{q}_3 q_1) \\ \dot{y} + 2R(\dot{q}_0 q_1 - \dot{q}_1 q_0 + \dot{q}_2 q_3 - \dot{q}_3 q_2) \end{bmatrix} = \mathbf{0} \end{aligned} \tag{5}$$

Applying the variational technique, we derive at the end the equations of motion in mode-dependent form as:

$$\begin{cases} \dfrac{d}{dt}\left(\dfrac{\partial \mathcal{L}}{\partial \dot{\boldsymbol{\eta}}}\right) - \dfrac{\partial \mathcal{L}}{\partial \boldsymbol{\eta}} = \dfrac{\partial \psi_q}{\partial \boldsymbol{\eta}}\lambda_q + \sigma\left(\dfrac{\partial \psi_c}{\partial \boldsymbol{\eta}}\lambda_c + \dfrac{\partial \boldsymbol{\psi}_r}{\partial \dot{\boldsymbol{\eta}}}\boldsymbol{\lambda}_r\right) + \boldsymbol{\tau} \\ \dfrac{d^2\psi_q}{dt^2} = 0 \\ \sigma\dfrac{d^2\psi_c}{dt^2} = 0 \\ \sigma\dfrac{d\boldsymbol{\psi}_r}{dt} = \mathbf{0} \end{cases}, \qquad \sigma = \begin{cases} 1, & \text{rolling} \\ 0, & \text{flying} \end{cases} \tag{6}$$

The scalar σ activates the contact and rolling constraints only in terrestrial locomotion. The flight model is obtained by setting $\sigma = 0$, thereby removing the ground-contact and pure-rolling constraints. In equations (6), $\boldsymbol{\tau} \in \mathbb{R}^7$ represents the generalized forces acting on the system and produced by the resultant of the aerodynamic actions of the eight rotors. These comprise the thrust forces f_{r_i} and the drag torques t_{r_i}, acting along the rotational axis $\vec{\mathbf{e}}_{r_i}$ of the corresponding i-th rotor. Being $\boldsymbol{d}_{r_i}$ represents the position of the i-th rotor with respect to the center of mass, the generalized action is:

$$\boldsymbol{\tau} = \begin{bmatrix} \displaystyle\sum_{i=1}^{8} f_{r_i}\vec{\mathbf{e}}_{r_i} \\ 2\boldsymbol{E}(\boldsymbol{q})\left(\displaystyle\sum_{i=1}^{8} \boldsymbol{d}_{r_i} \times f_{r_i}\vec{\mathbf{e}}_{r_i} + \sum_{i=1}^{8} t_{r_i}\vec{\mathbf{e}}_{r_i}\right) \end{bmatrix} \tag{7}$$

Bench tests of the motor–propeller unit showed that, within the operating range considered here and neglecting the rotor dynamics, the thrust generated by each rotor can be approximated as proportional to the corresponding aerodynamic torque:

$$f_{r_i} = s_i k t_{r_i}, \qquad s_i \in \{-1, +1\} \tag{8}$$

where k is an experimentally identified thrust to drag ratio coefficient and s_i accounts for the handedness of the rotor, distinguishing between clockwise and counterclockwise.
Consequently, the generalized actions introduced in (7) can be expressed in terms of the rotors aerodynamic torque vector $\boldsymbol{t}_r = \left[t_{r_1}, t_{r_2}, \dots, t_{r_8}\right]^\top$. Thus, the dynamic reference model defined in (6) can be reformulated in a first-order form affine in the control action:

$$\dot{\boldsymbol{x}} = \boldsymbol{\phi}(\boldsymbol{x}) + \boldsymbol{D}(\boldsymbol{x})\boldsymbol{t}_r \tag{9}$$

where $\boldsymbol{\phi}(\boldsymbol{x})$ characterizes the nonlinear dynamics and $\boldsymbol{D}(\boldsymbol{x})$ maps the eight rotor torques into generalized forces. Equation (9) serves as the affine model used to design the model-based controller described in the following section.

3.2 State Estimation and Contact Detection

The state estimation algorithm is based on a mode-dependent approach, in which an Extended Kalman Filter (EKF) [21] fuses onboard sensors measurements with a prediction model selected according to the operating mode. In flight, the filter adopts an inertial navigation model, in which state prediction is based on IMU measurements, while magnetometer, barometer, and GNSS provide corrections for heading, altitude, position, and velocity. This sensor fusion architecture is consistent with the one used in EKF estimators for PX4 autopilots [19]. During rolling locomotion, instead, the prediction model additionally exploits the pure-rolling constraint:

$$\dot{\boldsymbol{r}} = -\boldsymbol{\omega} \times \boldsymbol{d}_c \tag{10}$$

Where $\boldsymbol{d}_c = [0, 0, R]^\top$ is the position vector from the center of the sphere to the contact point. This constraint links translational velocity to angular velocity, providing an additional source of information during ground motion. As a result, horizontal position estimates can remain robust and consistent even when GNSS corrections are degraded or intermittent. Conversely, in flight mode, estimation performance remains critically dependent on GNSS integrity.

The active locomotion mode is detected by comparing the measured acceleration from the IMU with the flying-mode acceleration expected from the commanded rotor actions. The thrust-induced acceleration can be defined in body frame as:

$$\mathbf{a}_{th}^b = \frac{1}{m}\sum_{i=1}^{8} s_i \, kt_{r_i} \vec{\mathbf{e}}_{r_i}^b \ , \qquad s_i \in \{-1, +1\} \tag{11}$$

The contact residual is:

$$\Delta_c = \| \, \mathbf{a}_{th}^b - \mathbf{a}_{imu}^b \, \| \tag{12}$$

Then, the active operating mode is selected according to:

$$\text{mode} = \begin{cases} \text{rolling}, & \Delta_c > \varepsilon \\ \text{flying}, & \Delta_c \leq \varepsilon \end{cases} \tag{13}$$

Values of the residual exceeding the threshold ε indicate acceleration components not captured by the flight model, thus signifying external interactions such as ground contact. In preliminary experiments, conducted within a flat environment, the residual Δ_c remains centered around g during rolling locomotion, as the accelerometric measurements inherently include the gravitational contribution. Under these conditions, ground contact can be identified by filtering the contact residual and setting the threshold to $\varepsilon = g/2$. This logic has proven to provide a reliable switching signal with minimal false detections and chattering, establishing a baseline approach that can be further refined for more complex scenarios.

3.3 Nonlinear Feedback Control Law

At the core of ATHMOS's autonomous driving system lies a nonlinear control algorithm referred to as the Feedback Local Optimality Principle (FLOP), which enables the seamless integration of nonlinear behaviors typical of spherical omnidirectional control and contact dynamics. The controller computes the ideal actions to follow the desired trajectory $\boldsymbol{x}_T$. For implementation, the control variable is defined as a fictitious generalized action $\boldsymbol{u} \in \mathbb{R}^7$,

composed of three translational force components and four generalized rotational components associated with the quaternion coordinates.

Building on our previous work [14-16], the FLOP technique is briefly outlined below to illustrate its underlying principles. The method locally reformulates an optimal control problem for affine nonlinear systems of the form $\dot{\boldsymbol{x}} = \boldsymbol{\phi}(\boldsymbol{x}) + \boldsymbol{B}\boldsymbol{u}$, and derives an explicit state-feedback control law suitable for real-time execution. The objective is the simultaneous minimization of the trajectory tracking error and the associated control effort:

$$\min_{\boldsymbol{u}} J = \frac{1}{2}\int_0^T h(\boldsymbol{x}, \boldsymbol{x}_T) + (\boldsymbol{u} - \boldsymbol{u}_T)^\top \boldsymbol{R}(\boldsymbol{u} - \boldsymbol{u}_T)dt \qquad Subject\ to: \quad \dot{\boldsymbol{x}} = \boldsymbol{\phi}(\boldsymbol{x}) + \boldsymbol{B}\boldsymbol{u} \tag{14}$$

Here, $h(\boldsymbol{x}, \boldsymbol{x}_T)$ is a generic nonlinear differentiable function properly designed to express the trajectory tracking error, $\boldsymbol{u}_T$ is the target control action, and $\boldsymbol{R}$ is a positive-definite diagonal weighting matrix. Using the variational formulation and a local time discretization, the resulting state-feedback law can be written as:

$$\boldsymbol{u} = \boldsymbol{R}^{-\top}\boldsymbol{B}^\top \left[\frac{\partial \boldsymbol{\phi}(\boldsymbol{x})}{\partial \boldsymbol{x}}^\top - \frac{1}{\Delta t}\boldsymbol{I}\right]^{-1} \frac{\partial h(\boldsymbol{x}, \boldsymbol{x}_T)}{\partial \boldsymbol{x}}^\top + \boldsymbol{B}^+[\dot{\boldsymbol{x}}_T - \boldsymbol{\phi}(\boldsymbol{x}_T)] \tag{15}$$

Where Δt is a positive control parameter to be tuned together with the control gains contained in matrix $\boldsymbol{R}$; the superscript + denotes the Moore–Penrose pseudoinverse of matrix $\boldsymbol{B}$, which is suitably formulated to introduce the fictitious actions into the system model.

However, the standard FLOP formulation does not inherently account for constraints on the control variable, potentially leading to unattainable force and torque demands. To address this, the Constrained Allocation block maps the fictitious actions $\boldsymbol{u}$ into feasible rotor torques $\boldsymbol{t}_r$. At each time step, the constrained allocation solves an optimization problem using Quadratic Programming techniques, where the objective function consists of two main contributions. The first ensures dynamic equivalence between the ideal fictitious actions $\boldsymbol{u}$ and the effect produced by actual rotor torques $\boldsymbol{t}_r$, while the second acts as a smoothing term by penalizing abrupt variations relative to the previous command $\boldsymbol{t}_r^*$. Simultaneously, the solver enforces hard constraints on the rotor torques, keeping them within the actuators' physical bounds $\boldsymbol{t}_r^-$ and $\boldsymbol{t}_r^+$ identified from motor bench tests.

$$\min_{\boldsymbol{t}_m} \ \chi_1\|\boldsymbol{B}\boldsymbol{u} - \boldsymbol{D}\boldsymbol{t}_r\|^2 + \chi_2\|\boldsymbol{t}_r - \boldsymbol{t}_r^*\|^2 \qquad Subject\ to: \quad \boldsymbol{t}_r^- \le \boldsymbol{t}_r \le \boldsymbol{t}_r^+ \tag{16}$$

The final Conversion Map block converts the allocated rotor torques $\boldsymbol{t}_r$ into the corresponding PWM commands for the brushless motor ESCs. The mapping process is governed by the rotor's characteristic model illustrated in Figure 4, which was experimentally identified through static bench tests. This model accounts for real-time supply voltage V_{dc} compensation to determine the command signal for the i-th motor as follows:

$$PWM_i = \frac{1}{V_{dc}}\left(c_1 t_{r_i} + c_2\sqrt{|t_{r_i}|}\cdot sign(t_{r_i}) + c_3\right), \qquad PWM_i \in [-1,1] \tag{17}$$

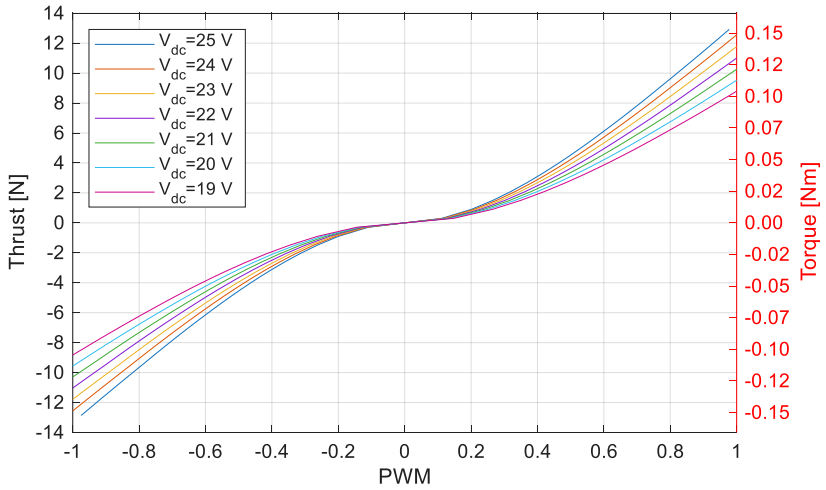


Figure 4: Model of the motor–propeller unit characteristics used to map the desired rotor action into PWM commands while accounting for supply-voltage variations.

4 EXPERIMENTAL VALIDATION

The proposed experimental campaign aims to demonstrate the ability of ATHMOS to robustly manage hybrid locomotion. Particular emphasis is placed on the mode transition phases, which are required to be responsive, smooth and resilient to landing-induced impacts. The robot was evaluated through trajectory tracking tasks across mixed flight and rolling segments in non-ideal outdoor environments, providing more significant testing conditions than controlled laboratory settings. The robot trajectory was reconstructed using videogrammetry from synchronized videos acquired from multiple viewpoints, providing a ground-truth reference for evaluating path tracking, estimator performance, and transition behavior.

4.1 Autonomous Rolling Test

Since rolling is intended to be the primary navigation mode for extended traverses, the first experiment evaluated autonomous ground tracking. The commanded path was a 4 x 4 m rectangular trajectory, repeated twice. The test was performed on rough stone paving and included a sloped section with an inclination of approximately 20%. This terrain was deliberately selected to include non-ideal contact conditions and local disturbances not explicitly modeled in the controller. Moreover, a non-smooth target velocity profile was intentionally assigned to further stress the operating conditions and evaluate the controller's robustness against aggressive reference changes, specifically at the corners of the path.

Tracking performance was evaluated through the cross-track error e_{XTE}, defined as the minimum Euclidean distance between the ground-truth position $\boldsymbol{r}(t_i)$ at sample time t_i and the reference path $\boldsymbol{r}_T$. The overall error was summarized through the root mean square error (RMSE) over the N collected data samples:

$$e_{XTE}(t_i) = \min\|\boldsymbol{r}(t_i) - \boldsymbol{r}_T\|$$

$$RMSE_{XTE} = \sqrt{\frac{1}{N}\sum_{i=1}^{N} e_{XTE}(t_i)^2}, \qquad \forall\, i \in [0, N] \tag{18}$$

As shown in Figure 5, the robot completed the two laps while maintaining the cross-track error below approximately 0.5 m. The resulting $RMSE_{XTE}$ value is about 0.24 m, despite the rough surface, slope, and GNSS degradation.

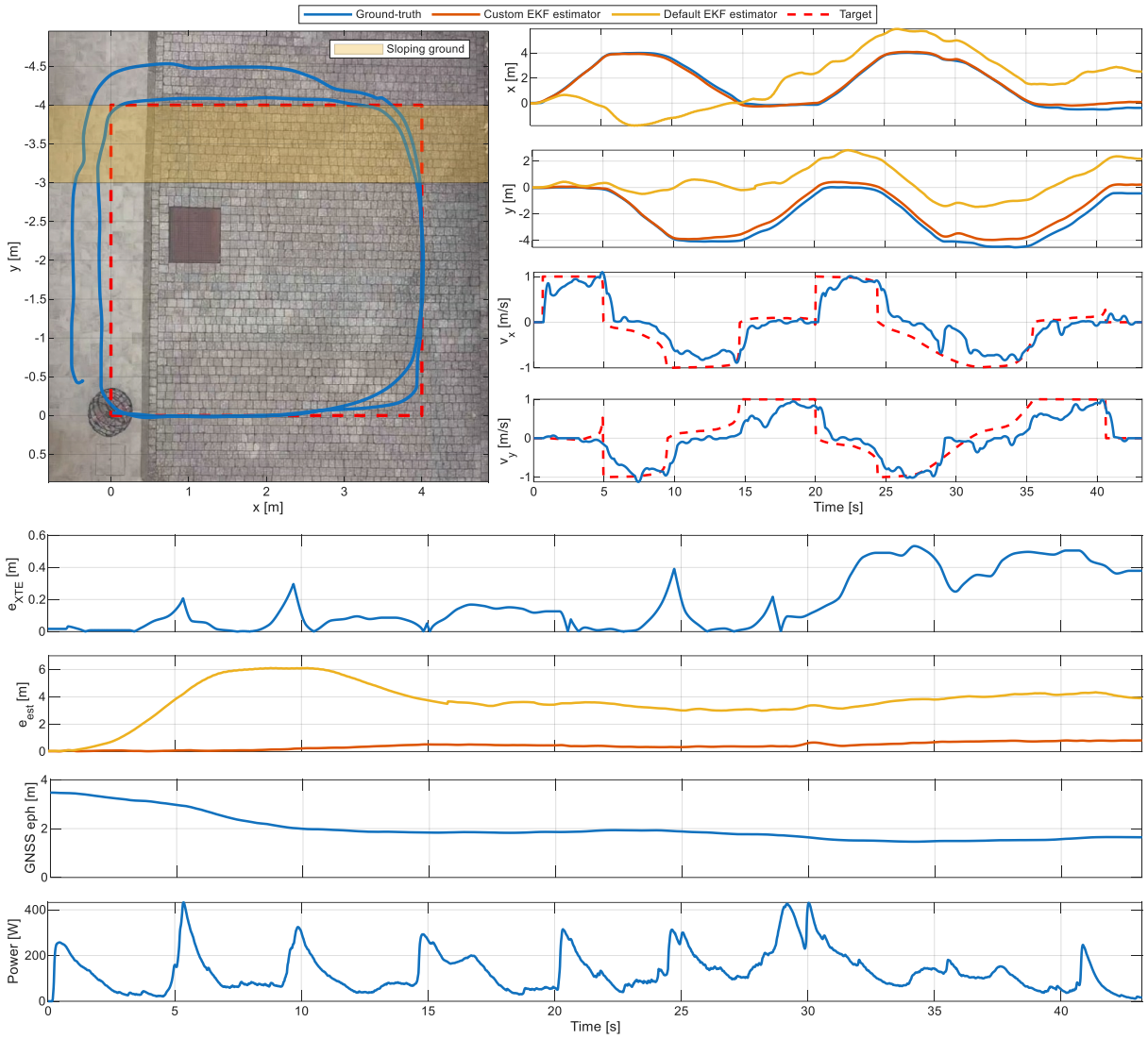


Figure 5: Autonomous rolling experiment on rough stone-paved terrain with a 20% sloped section. The figure reports the reference, reconstructed and estimated trajectories from the custom EKF estimator enforcing the rolling constraint and from the default EKF estimator provided by PX4. Accordingly, the cross-track error and horizontal position estimates are derived and plotted, along with GNSS horizontal accuracy and absorbed power.

In fact, this test also demonstrates the benefit of the custom EKF estimator enforcing the pure rolling constraint, with respect to the default EKF estimator provided by PX4. For both estimators, we evaluated the position estimation error e_{est} as the norm of the difference between the ground-truth position and the estimated position $\boldsymbol{r}_{est}$, and the corresponding root mean squared error value:

$$e_{est}(t_i) = \|\boldsymbol{r}(t_i) - \boldsymbol{r}_{est}(t_i)\|$$

$$RMSE_{est} = \sqrt{\frac{1}{N}\sum_{i=1}^{N} e_{est}(t_i)^2}, \qquad \forall\, i \in [0, N] \tag{19}$$

During the experiment, the GNSS horizontal position accuracy, expressed through the eph indicator, ranged between 1.5 m and 3.6 m. Under these conditions, the default PX4 estimator showed a $RMSE_{est}$ value of almost 4 m, while the custom EKF estimator reduced this value to

approximately 0.5 m. The main quantitative results about the performances in the autonomous rolling test are summarized in Table 1. At an average speed of about 0.7 m/s, the average absorbed power was approximately 130 W, with peaks up to 400 W during 90-degree turns and while climbing the sloped section.

Metric	Description	Value
$RMSE_{XTE}$	Root mean square of the cross-track error between ground-truth and reference path	0.24 m
$RMSE_{est}^{PX4}$	Root mean square of the horizontal position estimation error obtained with the default EKF estimator provided by PX4	3.94 m
$RMSE_{est}^{roll}$	Root mean square of the horizontal position estimation error obtained with the custom EKF estimator enforcing rolling constraint	0.48 m

Table 1: Quantitative performance metrics of the autonomous rolling test.

4.2 Mode Transition Test

The second experiment evaluated the ability of ATHMOS to handle transitions between terrestrial and aerial mode, that is a key feature for agile and versatile hybrid navigation. In this case, the target motion was manually assigned in real time by an operator that assigned a desired velocity profile in real time. The test was performed on rough grassy terrain, which is more compliant and irregular than the stone-paved surface used in the previous experiment.

As illustrated in Figure 6, the maneuver sequence consisted of three main operational phases. Initially, ATHMOS executed a rolling segment starting from rest, denoted by $t_1 \rightarrow t_2$. Then, the robot took off from a generic attitude $\boldsymbol{q}(t_2)$ and entered into flight mode; it converged to the desired attitude $\boldsymbol{q}_T$ by t_4, before approaching the landing phase within the timeframe $t_5 \rightarrow t_6$. Finally, after the ground impact, ATHMOS resumed rolling and decelerated to rest at t_7. The system exhibits agile and robust transitions, characterized by reactive attitude recovery during takeoff and effective contact impact management without loss of stability or dynamical discontinuities. The contact detection algorithm ensures responsive and precise mode switching identification: the impulsive nature of landing triggers near-instantaneous detection, while takeoff is identified with a negligible delay of 0.3 seconds. The characteristic response times of the system during mode transitions are reported in Table 2, demonstrating its high reactivity and agility.

Metric	Description	Value
Lift-off delay	Time elapsed between the take-off motor command and loss of ground contact	0.15 s
Attitude recovery time	Settling time required to reach the desired flight attitude after take-off	4.50 s
Flight-mode detection delay	Time elapsed between lift-off and detection of the flying mode	0.30 s
Rolling-mode detection delay	Time elapsed between ground contact and detection of rolling mode	0.04 s

Table 2: Transition performance metrics measured during the mode transition experiment. The results quantify the responsiveness of the vehicle during lift-off, attitude recovery, and contact-based mode detection.

Furthermore, the rotor thrust profiles remain smooth, without aggressive oscillations. Energetic analysis reveals that rolling on grass requires an average power of 250 W, an 82% reduction compared to the 1420 W required for flight, confirming the high advantages of hybrid locomotion for extended operations.

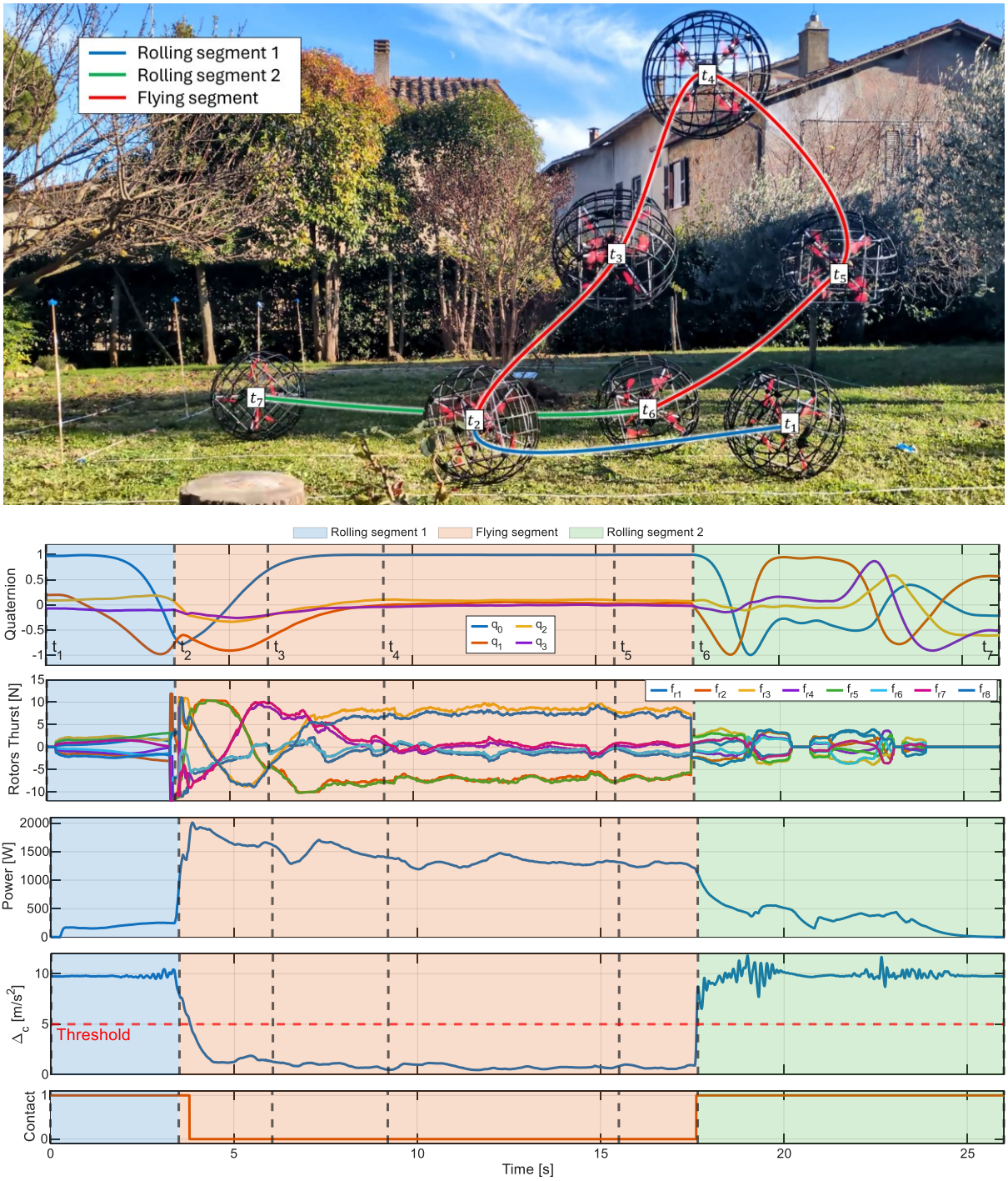


Figure 6: Rolling–flying–rolling transition experiment on rough grassy terrain. The top panel shows the reconstructed trajectory during the maneuver sequence t_1–t_7. The lower panels report quaternion evolution, rotor thrusts, absorbed power, contact-detection residual, and detected locomotion mode

4.3 Energetic Analysis

To compare the energetic efficiency of rolling and flight independently of travel distance of different missions, the cost of transport was used:

$$COT = \frac{E}{mgd} = \frac{\bar{P}}{mg\bar{V}} \tag{20}$$

where E is the energy consumed over distance d, m is the transported mass, $\bar{P}$ is the average absorbed power, and $\bar{V}$is the average transport velocity. Table 3 summarizes the results obtained in different operating conditions, including the two previously discussed experiments and an additional representative test case. Rolling on rough stone-paved terrain required the lowest cost of transport, with $COT = 7$. Rolling on grassy terrain was more dissipative, especially at lower speed, but still remained below $COT = 16$. Flight showed substantially higher values, between 102 and 158 in the tested low-speed conditions.

Test	Mode	Ground type	Average Power	Average Velocity	COT
1	Rolling	Rough stone-paved surface	128 W	0.7 m/s	7
2	Rolling	Rough grassy terrain	250 W	0.6 m/s	16
3	Rolling	Rough grassy terrain	550 W	1.7 m/s	12
2	Flying	-	1420 W	0.34 m/s	158
3	Flying	-	1350 W	0.5 m/s	102

Table 3: Energy comparison between rolling and flight in the tested operating conditions.

The measured values confirm the central motivation behind the ATHMOS architecture. Rolling is substantially more efficient than flight for extended motion, even on irregular grassy terrain. The efficiency advantage ranges from approximately 6 to 23 times in the reported tests: it is higher on less dissipative surfaces but remains significant in rougher outdoor conditions. The table also shows the effect of speed: within the tested range, higher rolling velocity can improve transport efficiency by exploiting the inertia of the spherical body, provided that the maneuver does not require aggressive accelerations or repeated sharp turns.

5 CONCLUSION

This paper presented the experimental validation of ATHMOS, a hybrid aerial–terrestrial robot that combines an overactuated eight-rotor propulsion system with a rigid external spherical shell. Field tests in unstructured outdoor environments demonstrate that the synergy between its specialized mechanical design and dedicated estimation and control architecture enables the integration of effective hybrid locomotion within a compact platform. The results show autonomous trajectory-tracking capabilities over mixed aerial–ground segments, with agile and seamless mode transitions, including take-off from arbitrary rolling attitudes, stable landings, and reliable ground-contact detection. The experiments also quantify the significant energetic advantage of rolling locomotion, supporting the adopted navigation strategy where terrestrial motion is used for long-distance traverses and rapid switching to flight is reserved for overcoming obstacles or tridimensional maneuvers. In this way, ATHMOS preserves the agility of an aerial system while substantially improving the overall energetic efficiency of the navigation. A particularly relevant outcome is the contribution of the pure-rolling kinematic constraint within the EKF-based state estimator. Compared with standard inertial navigation-based EKF estimators, the proposed approach significantly improves the robustness and con-

tinuity of state estimation under degraded GNSS conditions, which is crucial for autonomous operation in unstructured environments. Overall, the experimental campaign validates the main performance hypotheses identified in the previous numerical study and provides a solid experimental basis for future developments. These will focus on hardware optimization, broader testing in more complex operational scenarios, and the enhancement of autonomous navigation capabilities through an expanded sensor suite and advanced planning algorithms.

REFERENCES

[1] B. Hu, Z. Dong and L. Zhang. “Land-Air Amphibious Robots: A Survey”. In: *Artificial Intelligence*. Ed. by L. Fang, J. Pei, G. Zhai and R. Wang. Singapore: Springer Nature Singapore, 2024, pp. 575–586.

[2] S. Mintchev and D. Floreano. “A multi-modal hovering and terrestrial robot with adaptive morphology”. In: *Proceedings of the 2nd International Symposium on Aerial Robotics*. 2018.

[3] R. Zhang, Y. Wu, L. Zhang, C. Xu and F. Gao. “Autonomous and Adaptive Navigation for Terrestrial-Aerial Bimodal Vehicles”. In: *IEEE Robotics and Automation Letters* 7.2 (2022), pp. 3008–3015. DOI: 10.1109/LRA.2022.3145505.

[4] N. Pan, J. Jiang, R. Zhang, C. Xu and F. Gao. “Skywalker: A Compact and Agile Air-Ground Omnidirectional Vehicle”. In: *IEEE Robotics and Automation Letters* 8.5 (2023), pp. 2534–2541. DOI: 10.1109/LRA.2023.3256920.

[5] H. Jia, R. Ding, K. Dong, S. Bai and P. Chirarattananon. “Quadrolltor: A Reconfigurable Quadrotor With Controlled Rolling and Turning”. In: *IEEE Robotics and Automation Letters* 8.7 (2023), pp. 4052–4059. DOI: 10.1109/LRA.2023.3279624.

[6] A. Kalantari and M. Spenko. “Modeling and Performance Assessment of the HyTAQ, a Hybrid Terrestrial/Aerial Quadrotor”. In: *IEEE Transactions on Robotics* 30.5 (2014), pp. 1278–1285. DOI: 10.1109/TRO.2014.2337555.

[7] Y. Yao, Z. Deng, X. Zhang and C. Lv. “Design and Implementation of a Quadrotor-Based Spherical Robot”. In: *Proceedings of the 2021 IEEE 5th Advanced Information Technology, Electronic and Automation Control Conference (IAEAC)*. 2021, pp. 2430–2434. DOI: 10.1109/IAEAC50856.2021.9391066.

[8] C. J. Dudley, A. C. Woods and K. K. Leang. “A micro spherical rolling and flying robot”. In: *Proceedings of the 2015 IEEE/RSJ International Conference on Intelligent Robots and Systems (IROS)*. 2015, pp. 5863–5869. DOI: 10.1109/IROS.2015.7354210.

[9] A. Khalil, M. A. Jaradat, S. Mukhopadhyay and M. F. Abdel-Hafez. “Autonomous Control of a Hybrid Rolling and Flying Caged Drone for Leak Detection in HVAC Ducts”. In: *IEEE/ASME Transactions on Mechatronics* 29.1 (2024), pp. 366–378. DOI: 10.1109/TMECH.2023.3279870.

[10] A. Briod, P. Kornatowski, J.-C. Zufferey and D. Floreano. “A Collision-resilient Flying Robot”. In: *Journal of Field Robotics* 31.4 (2014), pp. 496–509. DOI: 10.1002/rob.21495.

[11] S. Atay, M. Bryant and G. Buckner. “The Spherical Rolling-Flying Vehicle: Dynamic Modeling and Control System Design”. In: *Journal of Mechanisms and Robotics* 13.5 (2021). DOI: 10.1115/1.4050831.

[12] I. Miura, B. Zhang and H. O. Lim. “A High Safety Spherical Flying Robot based on Gimbal Mechanism”. In: *Proceedings of the 2022 9th International Conference on Dependable Systems and Their Applications (DSA)*. 2022, pp. 1006–1007. DOI: 10.1109/DSA56465.2022.00146.

[13] S. Sabet, A. A. Agha-Mohammadi, A. Tagliabue, D. S. Elliott and P. E. Nikravesh. “Rollocopter: An Energy-Aware Hybrid Aerial-Ground Mobility for Extreme Terrains”. In: *Proceedings of the 2019 IEEE Aerospace Conference*. 2019, pp. 1–8. DOI: 10.1109/AERO.2019.8741685.

[14] G. Pepe, D. Antonelli, L. Nesi and A. Carcaterra. “FLOP: Feedback local optimality control of the inverse pendulum oscillations”. In: *Proceedings of ISMA 2018 - International Conference on Noise and Vibration Engineering and USD 2018 - International Conference on Uncertainty in Structural Dynamics*. 2018, pp. 93–106.

[15] G. Pepe, M. Laurenza, D. Antonelli and A. Carcaterra. “A new optimal control of obstacle avoidance for safer autonomous driving”. In: *Proceedings of the 2019 AEIT International Conference of Electrical and Electronic Technologies for Automotive (AEIT AUTOMOTIVE)*. 2019. DOI: 10.23919/EETA.2019.8804549.

[16] D. Spitaleri, G. Pepe, M. Laurenza, S. Milana and A. Carcaterra. “Enhancing Spherical Rolling Robot Control for Slippery Terrain”. In: *Proceedings of the 2024 13th International Workshop on Robot Motion and Control (RoMoCo)*. 2024, pp. 243–248. DOI: 10.1109/RoMoCo60539.2024.10604310.

[17] D. Spitaleri, G. Pepe, M. Laurenza, S. Milana, F. Ceccarelli and A. Carcaterra. “Advanced Nonlinear Control for an Omnidirectional Spherical Robot Integrating Aerial and Ground Mobility”. In: *Proceedings of the 21st International Conference on Informatics in Control, Automation and Robotics (ICINCO 2024)*. 2024, pp. 684–691. DOI: 10.5220/0013020300003822.

[18] D. Brescianini and R. D’Andrea. “An omni-directional multirotor vehicle”. In: *Mechatronics* 55 (2018), pp. 76–93. DOI: 10.1016/j.mechatronics.2018.08.005.

[19] PX4 Autopilot Development Team. PX4 Autopilot: Open Source Autopilot for Drones. Online. 2026. URL: https://px4.io/ (visited on 30.04.2026)

[20] P. E. Nikravesh, R. A. Wehage and O. K. Kwon. “Euler Parameters in Computational Kinematics and Dynamics. Part 1”. In: *Journal of Mechanisms, Transmissions, and Automation in Design* 107.3 (1985), pp. 358–365. DOI: 10.1115/1.3260722.

[21] D. Simon. *Optimal State Estimation: Kalman, H Infinity, and Nonlinear Approaches*. Hoboken, NJ: Wiley, 2006. ISBN: 978-0-471-70858-2.